

Adjoint-based Limit Cycle Oscillation Instability Sensitivity and Suppression

Sicheng He (✉ hschsc@umich.edu)

University of Michigan <https://orcid.org/0000-0003-1307-4909>

Eirikur Jonsson

University of Michigan

Joaquim R. R. A. Martins

University of Michigan

Research Article

Keywords: Adjoint method, LCO, Stability, Time spectral method, Gradient-based optimization

Posted Date: February 21st, 2022

DOI: <https://doi.org/10.21203/rs.3.rs-1328145/v1>

License: © ⓘ This work is licensed under a Creative Commons Attribution 4.0 International License.

[Read Full License](#)

Adjoint-based Limit Cycle Oscillation Instability Sensitivity and Suppression

Sicheng He, Eirikur Jonsson, Joaquim R. R. A. Martins

Received: date / Accepted: date

Abstract Limit cycle oscillations (LCO) can be supercritical or subcritical. The supercritical response is benign, while the subcritical response can be destructive. It is desirable to avoid subcritical responses by enforcing LCO stability through design optimization constraints. However, there is a need for a computational approach that can model this instability and can handle hundreds or thousands of design variables. We propose a simple metric to determine the LCO stability using a fitted bifurcation diagram slope to address this need. We develop an adjoint-based formula to compute the stability derivative efficiently with respect to many design variables. To evaluate the stability derivative, we only need to compute the time-spectral adjoint equation three times no matter the number of design variables in the optimization problem. The proposed adjoint method is verified with finite differences, achieving a five-digit agreement between the two approaches. We consider a stability-constrained LCO parameter optimization problem and demonstrate that the optimizer can suppress the instability. Finally, we consider a more realistic LCO speed and stability-constrained mass minimization problem for an airfoil. The proposed method can be extended to optimization problems with a PDE-based model, opening the door to applications where high-fidelity models are needed.

Keywords Adjoint method · LCO · Stability · Time spectral method · Gradient-based optimization

Sicheng He, E-mail: hschsc@umich.edu
Eirikur Jonsson, E-mail: eirikurj@umich.edu
Joaquim R. R. A. Martins, E-mail: jrram@umich.edu

Aerospace Engineering, University of Michigan,
François-Xavier Bagnoud Aerospace Building, 1320 Beal Avenue, Ann Arbor, MI 48109-2140

1 Introduction

Limit cycle oscillation (LCO) is frequently encountered in engineering applications, such as, aeroelastics (Thomas et al., 2002; Huang et al., 2018; He et al., 2019a; Li and Ekici, 2019; Jonsson et al., 2019; Riso et al., 2020), bipedal robotics (Grizzle et al., 2001; Shiriaev et al., 2008; Manchester et al., 2011), and combustion (Waugh et al., 2014; Xu et al., 2020). In the context of design optimization, the scalability of computational cost with respect to the number of design variables is essential for problems with a large number of design variables and with a PDE governing equation. The adjoint method can compute the derivative with a computational cost independent of the number of design variables (Jameson, 1988). From the perspective of dynamical system, using adjoint method, significant progress has been made in fixed point problem (Jameson, 1988; Kenway et al., 2014, 2019; Shi et al., 2020), LCO (Thomas and Dowell, 2019; He et al., 2019a), and chaotic dynamical system (Wang, 2013; Shimizu and Fidkowski, 2016; Lasagna, 2018).

For derivatives related to LCO, most of the previous research focused on the derivative of LCO parameters, such as amplitude, phase, or period (Wilkins et al., 2009; Thomas and Dowell, 2019; He et al., 2019a). The stability of LCO and its derivative are also critical characteristics. The LCO stability, or periodic system stability, is traditionally evaluated using the Floquet theory (Floquet, 1883; Friedmann et al., 1977; Chicone, 2006). It states that the stability of a periodic dynamical system is determined by the eigenvalue distribution of the monodromy matrix. The monodromy matrix is obtained by evaluating the fundamental solution matrix of the periodic system at $t = 0$ and $t = T$, where t is the time and T is one period of the system (see Chapter 2.4 of the textbook by Chicone (2006)). In practice, the monodromy matrix is obtained by simulating the time-periodic dynamical system N times for one period, where N is the number of states of the dynamical system. This is prohibitively expensive for problems governed by a PDE, in particular when N is large, such as the high-fidelity aeroelastic systems considered by Thomas et al. (2002); He et al. (2019a). Furthermore, Bauchau and Nikishkov (2001) realized that it is possible to use the Arnoldi algorithm to compute the dominant eigenvalue, instead of computing all eigenvalues to determine the stability of a periodic dynamical system. This approach is appealing because the matrix is never formed explicitly; only matrix-vector products are required by the Arnoldi algorithm, where the response vector can be evaluated using a time integration for one period for a given initial condition. However, to compute the derivative of this approach efficiently, an unsteady adjoint (Cao et al., 2003) is necessary, which requires significant development effort and computational time. The Floquet analysis was differentiated in the forward mode by Seyranian et al. (2000). However, the computational cost of such a derivative computation method scales with the number of design variables. Recently, Riso et al. (2021) proposed an approximate recovery rate as a metric for post-flutter analysis and gradient-based optimization that avoids the otherwise expensive transient simulation necessary. The method is demonstrated in a simple optimization problem on a typical airfoil section, minimizing the mass ratio, subject to flutter and the proposed post-flutter constraint. The proposed method successfully eliminates any subcritical characteristics.

To mitigate the computational cost and implementation challenges encountered when applying the Floquet theory, we propose a bifurcation diagram-based fitting method to capture the instability and an adjoint method to evaluate the derivative of the instability metric efficiently with respect to the design variables. A third-order polynomial is fitted by sampling a total of three post bifurcation points and enforcing the intersection angle with the parameter axis at the Hopf-point to be 90° . In principle, the sampling points can be computed using various approaches, but in this work, they are evaluated by solving the so-called time-spectral LCO equation (Thomas et al., 2002; He et al., 2019b, 2021). The slope is used as a metric to determine stability. The derivative of the stability metric is then computed using the adjoint method. The fitted curve adjoint requires the solution of the so-called time spectral LCO adjoint (Thomas and Dowell, 2019; He et al., 2019a) for all three points. This is the first time the time spectral method has been applied for LCO optimization with the stability constraint. The method can potentially be extended to solving high-fidelity optimization problems because the derivative computational cost is independent of the number of design variables.

The paper is organized as follows. In Section 2, we gave an overview of the problem and optimization setup. In Section 3, we discuss the governing time spectral equations used for LCO computation. The proposed fitted curve-based stability criterion is presented in Section 4, followed by Section 5, detailing the adjoint equations used to compute the underlying LCO parameter derivative and the formula to compute the stability derivative. Then, in Section 6, we test the analysis algorithm by comparing the adjoint derivative with finite differences. We consider an optimization problem maximizing the LCO parameter while also ensuring the system is stable. We then consider a more practical LCO parameter- and stability-constrained airfoil mass minimization problem. In this problem, we aim to minimize the weight of an airfoil, and thus, leave more weight for the payload. However, by doing so, the structure may potentially become more flexible and prone to LCO at a lower air speed. We constrain the LCO parameter (in this case, air speed) and LCO stability to avoid this. Finally, we present our conclusions in Section 7.

2 Problem setup

This section provides an overview of the problem setup and optimization problem statement. A dynamic system can be described by the following general equation:

$$\frac{d\mathbf{w}}{dt} = \mathbf{f}(\mu, \mathbf{w}(\mathbf{x}), \mathbf{x}), \quad (1)$$

where $\mathbf{f}: \mathbb{R}^N \rightarrow \mathbb{R}^N$ is some nonlinear function, $\mu \in \mathbb{R}$ is the LCO parameter, and $\mathbf{w}(\mathbf{x}) \in \mathbb{R}^N$ is the vector of state variables. Also, when the motion magnitude approaches to zero, μ is also equal to the bifurcation parameter. The state variables depend on the design variable vector, $\mathbf{x} \in \mathbb{R}^{n_x}$, where n_x is the number of design variables, and N is the dimension of the state space.

The optimization problem is formulated as follows:

$$\begin{aligned}
& \text{minimize} && -\mu(\mathbf{x}) \\
& \text{by varying} && \mathbf{x}, \\
& \text{subject to} && g_{\text{stab}}(\mathbf{x}) > \hat{g}, \\
& && \underline{\mathbf{x}} \leq \mathbf{x} \leq \bar{\mathbf{x}},
\end{aligned} \tag{2}$$

where $g_{\text{stab}}(\mathbf{x})$ is the stability constraint, \hat{g} is a non-negative real number that can be tuned to make sure the dynamical system is stable, and $\underline{\mathbf{x}}$ and $\bar{\mathbf{x}}$ are the lower and upper bound vectors for the design variable, \mathbf{x} , respectively. Here $g_{\text{stab}}(\mathbf{x})$ is a scalar since only one operation condition is considered. When a multipoint optimization is conducted, we can use a vector to store the stability of all points that need to be constrained.

It is also possible to choose a different objective function to be optimized and set both the LCO stability and the LCO parameter as constraints. In this case, the problem is formulated as follows,

$$\begin{aligned}
& \text{minimize} && f(\mathbf{x}), \\
& \text{by varying} && \mathbf{x}, \\
& \text{subject to} && g_{\text{stab}}(\mathbf{x}) > \hat{g}, \\
& && \mu(\mathbf{x}) \geq \underline{\mu}, \\
& && \underline{\mathbf{x}} \leq \mathbf{x} \leq \bar{\mathbf{x}},
\end{aligned} \tag{3}$$

where $f(\mathbf{x})$ is the objective function and $\underline{\mu}$ is a lower bound for the LCO parameter.

3 Time spectral LCO equation

The time spectral LCO equation was first proposed by Thomas et al. (2002). It comprises a time spectral dynamic equation, motion magnitude, and phase equation. The motivation behind the motion magnitude is illustrated in Fig. 1. The magnitude constraint intersects with the bifurcation diagram and makes the solution unique. The fundamental idea of the time spectral method is to approximate a periodic dynamical system using several equally-spaced time snapshots. The temporal residual is computed by first computing the Fourier coefficient of the periodic state variables, evaluating the time derivative in the frequency domain, and converting it back to the time domain snapshots. The spatial residual is computed in the time domain.

The dynamic system, Eq. (1), can be cast into time-spectral form as follows. We write the LCO equation in residual form as

$$\begin{aligned}
\mathbf{R}_{\text{dyn}} &= \mathbf{w}^n - \begin{bmatrix} \mathbf{f}(\mu, \mathbf{w}_1) \\ \vdots \\ \mathbf{f}(\mu, \mathbf{w}_n) \end{bmatrix} \\
&= (\mathbf{P}^T \mathbf{D}^N(\omega) \mathbf{P}) \mathbf{w}^n - \begin{bmatrix} \mathbf{f}(\mu, \mathbf{w}_1) \\ \vdots \\ \mathbf{f}(\mu, \mathbf{w}_n) \end{bmatrix},
\end{aligned} \tag{4}$$

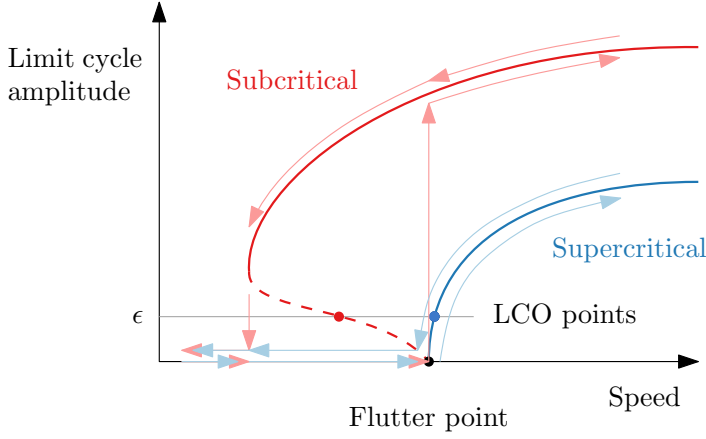


Fig. 1: Bifurcation diagram for systems with subcritical and supercritical responses.

where $\mathbf{w}^n \in \mathbb{R}^{n \times N}$ represents the state variables for all time instances, \mathbf{w}_i are the states for the i^{th} time instance, and ω is the angular velocity defined as $\omega = 2\pi/T$. The matrix \mathbf{P} is a permutation matrix defined as

$$\mathbf{P}_{i,j} = \begin{cases} 1 & \text{if } \text{mod}(j, N) = [i/n] \\ 0 & \text{otherwise} \end{cases}. \quad (5)$$

The matrix \mathbf{D}^N is composed of N spectral differentiation matrices on the diagonal and is given by

$$\mathbf{D}^N(\omega) = \begin{bmatrix} \mathbf{D} & 0 & \dots & 0 \\ 0 & \mathbf{D} & \ddots & 0 \\ \vdots & \ddots & \mathbf{D} & 0 \\ 0 & \dots & 0 & \mathbf{D} \end{bmatrix}, \quad \mathbf{D}_{i,j}(\omega) = \begin{cases} \frac{\omega(-1)^{(j-i)}}{2 \sin(\pi(j-i)/n)}, & \text{if } i \neq j, \\ 0, & \text{if } i = j, \end{cases}. \quad (6)$$

where $i, j = 1, \dots, n$. Here, we have N matrix blocks of \mathbf{D} on the diagonal.

In addition to the LCO equations, we constrain the magnitude and phase of the motion of one DOF. In residual form this can be written as,

$$\begin{aligned} R_m(\mathbf{w}^n) &= |\hat{\mathbf{w}}_1| - \hat{\alpha} = 0, \\ R_p(\mathbf{w}^n) &= \phi(\hat{\mathbf{w}}_1) - \hat{\phi} = 0, \end{aligned} \quad (7)$$

where $|\hat{\mathbf{w}}_1|$ is the motion magnitude of the first DOF from \mathbf{w}^n , ϕ is the phase of the motion, and $\hat{\alpha}, \hat{\phi}$ are the prescribed motion magnitude and phase, respectively. Here, $\hat{\mathbf{w}}_1$ is the state variables for all the first DOF. He et al. (2021) provides more details on how the motion magnitude and phase constraints are implemented.

Combining Eq. (4) and Eq. (7), the full system of equations becomes

$$\mathbf{R}(\mathbf{q}) = \begin{bmatrix} R_m(\mathbf{w}^n) \\ R_p(\mathbf{w}^n) \\ \mathbf{R}_{\text{dyn}}(\mu, \omega, \mathbf{w}^n) \end{bmatrix} = 0, \quad (8)$$

where \mathbf{q} is the state vector defined as

$$\mathbf{q} = \begin{bmatrix} \mu \\ \omega \\ \mathbf{w}^n \end{bmatrix}. \quad (9)$$

This system can be solved by segregated Newton–Raphson method (Thomas et al., 2002), or by a coupled Newton–Krylov method (He et al., 2021, 2019b). In this work, we use the latter. Newton-type methods are appealing because of their quadratic convergence rate property. However, all Newton-type methods require the initial point to be within the basin-of-attraction to converge, which often leads to issues with solution robustness. In the following sections, we discuss our proposed solution strategy.

3.1 Jacobian-free Newton–Krylov method

In this work, we apply a coupled Jacobian-free Newton–Krylov method to solve Eq. (8). The Newton increment $\Delta\mathbf{q}$ is computed by solving the following equation:

$$\mathbf{J}(\mathbf{q}^{(k)})\Delta\mathbf{q} = -\mathbf{R}(\mathbf{q}^{(k)}), \quad (10)$$

where \mathbf{J} is the Jacobian matrix of Eq. (8), and $\mathbf{q}^{(k)}$ is the solution from the k^{th} iteration. The updated state approximation is defined as

$$\mathbf{q}^{(k+1)} = \mathbf{q}^{(k)} + \theta\Delta\mathbf{q}, \quad (11)$$

where θ is determined by the line search.

When applying a Krylov subspace method to solve Eq. (10), only matrix–vector products are required. The product can be approximated by directional finite difference

$$\mathbf{J}(\mathbf{q}^{(k)})\mathbf{v} \approx \frac{\mathbf{R}(\mathbf{q}^{(k)} + \varepsilon\mathbf{v}^{(k)}) - \mathbf{R}(\mathbf{q}^{(k)})}{\varepsilon}, \quad (12)$$

thus never explicitly forming and storing the Jacobian. He et al. (2021) provides more details on the solver and preconditioners used to obtain the Newton increment in Eq. (10). In this work, we use the Scipy (Virtanen et al., 2020) implementation of the Jacobian-free Newton–Krylov method (Knoll and Keyes, 2004).

3.2 Warm-start strategy based on Hopf bifurcation analysis

Newton-type methods require the initial point to be reasonably close to the final solution to converge robustly. However, determining or finding a suitable initial point can be challenging and problem-dependent. Globalization methods that address the issue of robustness do exist, e.g., approximate Newton–Krylov (ANK) Yildirim et al. (2019), but such approach is not implemented here. Initialization with a prescribed motion is usually sufficient for a simple problem. However, this initialization strategy is insufficient for a more complex problem and requires a better strategy. Here we

implement a warm-start strategy, proposed by Thomas et al. (2002), where the initial point is based on a Hopf bifurcation analysis.

The idea is that we first linearize the Eq. (1) around a steady solution for certain μ . We decompose the state variable into a steady component and a perturbed state

$$\mathbf{w} = \bar{\mathbf{w}} + \delta\mathbf{w}, \quad (13)$$

where $\bar{\mathbf{w}}$ is a steady solution and $\delta\mathbf{w}$ is a perturbed state. Inserting the decomposed state into Eq. (1) we obtain

$$\frac{d(\bar{\mathbf{w}} + \delta\mathbf{w})}{dt} = \mathbf{f}(\mu, \bar{\mathbf{w}} + \delta\mathbf{w}). \quad (14)$$

Linearizing about the steady component of the state we obtain,

$$\mathbf{f}(\mu, \bar{\mathbf{w}} + \delta\mathbf{w}) = \mathbf{f}(\mu, \bar{\mathbf{w}}) + \mathbf{J}_{\text{dyn}}(\mu, \bar{\mathbf{w}})\delta\mathbf{w} + \text{H.O.T}(\delta\mathbf{w}). \quad (15)$$

It follows that the steady solution, $\bar{\mathbf{w}}$, satisfies

$$\mathbf{f}(\mu, \bar{\mathbf{w}}) = 0, \quad (16)$$

and the perturbed state variable $\delta\mathbf{w}$ satisfies

$$\frac{d\delta\mathbf{w}}{dt} = \mathbf{J}_{\text{dyn}}(\mu, \bar{\mathbf{w}})\delta\mathbf{w} + \text{H.O.T}(\delta\mathbf{w}). \quad (17)$$

The Jacobian matrix is defined as

$$\mathbf{J}_{\text{dyn}}(\mu, \bar{\mathbf{w}}) = \frac{\partial \mathbf{f}}{\partial \mathbf{w}}(\mu, \bar{\mathbf{w}}). \quad (18)$$

We can now identify the bifurcation point from the eigenvalues of the Jacobian matrix. The eigenmode of the solution $\delta\mathbf{w}$ takes the form

$$\delta\mathbf{w} = e^{\lambda t} \delta\tilde{\mathbf{w}}, \quad (19)$$

where λ is the eigenvalue and $\delta\tilde{\mathbf{w}}$ is the eigenvector. Inserting Eq. (19) into Eq. (17) and ignoring the higher order terms, we obtain

$$\mathbf{J}_{\text{dyn}}(\mu, \bar{\mathbf{w}})\delta\tilde{\mathbf{w}} = \lambda \delta\tilde{\mathbf{w}}. \quad (20)$$

The bifurcation happens when the maximum real part (the damping) of one conjugate pair of the eigenvalues is equal to zero, that is,

$$\max_j \text{Re}(\lambda_j(\mathbf{J}_{\text{dyn}}(\mu, \bar{\mathbf{w}}))) = 0. \quad (21)$$

We denote the steady solution of Eq. (16) at the bifurcation point as

$$\mu_{\text{bif}}, \bar{\mathbf{w}}_{\text{bif}}. \quad (22)$$

Similarly, we denote the eigenpair for the eigenvalue problem, Eq. (20), at the bifurcation point as

$$\lambda_{\text{bif}}, \delta\tilde{\mathbf{w}}_{\text{bif}}, \quad (23)$$

where $\text{Re}(\lambda_{\text{bif}}) = 0$. There are multiple ways to solve for μ_{bif} . One way is to define a search range and use bisection to find μ_{bif} .

After the bifurcation problem is solved, we can use the solution to initialize the time spectral LCO solver. The process to convert an eigenvalue problem solution to an initial point for the time spectral LCO solver is detailed in Algorithm 1. The output $\mathbf{q}^{(0)}$ is the initial solution found by this warm-start strategy.

Algorithm 1 Warm-start strategy using the bifurcation point solution

```

1: function  $\mathbf{f}_{\text{init}}(\mu_{\text{bif}}, \bar{\mathbf{w}}_{\text{bif}}, \lambda_{\text{bif}}, \delta \bar{\mathbf{w}}_{\text{bif}}, \hat{\alpha}, \hat{\phi})$ 
2:    $\mu^{(0)} \leftarrow \mu_{\text{bif}}$  ▷ Initialize the LCO parameter.
3:    $\omega^{(0)} \leftarrow |\text{Im}(\lambda_{\text{bif}})|$  ▷ Initialize the frequency.
4:    $\mathbf{w}^{n(0)} \leftarrow 0$  ▷ Allocate and initialize the displacement.
5:    $\mathbf{q}^{(0)} \leftarrow 0$  ▷ Allocate and initialize the state variables.
6:   for  $i = 1; i \leq n; i++$  do ▷ Traverse the time instances.
7:     for  $j = 1; j \leq N; j++$  do ▷ Traverse the DOFs.
8:        $\Delta_{\phi,j} = \phi(\delta \mathbf{w}_{\text{bif},j}) - \phi(\delta \mathbf{w}_{\text{bif},1})$  ▷ Compute the phase difference.
9:        $\phi_{i,j} = 2\pi \frac{i-1}{n} + \hat{\phi} + \Delta_{\phi,j}$  ▷ Compute the phase.
10:       $\gamma_j \leftarrow \frac{|\delta \mathbf{w}_{\text{bif},j}|}{|\delta \mathbf{w}_{\text{bif},1}|}$  ▷ Compute the magnitude ratio.
11:       $\mathbf{w}_{i,j}^{n(0)} \leftarrow \bar{\mathbf{w}}_{\text{bif},j} + \gamma_j \hat{\alpha} \sin \phi_{i,j}$  ▷ Compute the state variable.
12:    end for
13:  end for
14:   $\mathbf{q}^{(0)} \leftarrow (\mu^{(0)}, \omega^{(0)}, \mathbf{w}^{n(0)})$  ▷ Stack the initial state variables.
15: return  $\mathbf{q}^{(0)}$ 
16: end function

```

4 Stability criterion via fitted bifurcation diagram

The stability of an LCO point can be determined by the slope of its bifurcation diagram. For a bifurcation diagram with $\mu < \mu_{\text{bif}}$ the steady solution is stable, we have

$$\frac{d\hat{\alpha}}{d\mu} > 0, \quad (24)$$

indicates that the LCO is stable; if otherwise, $d\hat{\alpha}/d\mu < 0$, the system is unstable; and $d\hat{\alpha}/d\mu = 0$ is a critical point. We assume that when $\mu < \mu_{\text{bif}}$ the steady solution is stable because, otherwise, by defining μ as $-\mu$, the conclusion will be the opposite.

This assumption can usually be met in physical problems. For example, for aeroelastic LCO where μ can be chosen as the airspeed, we know that the steady solution is stable when the airspeed is low. This can also be verified by checking the Jacobian of a steady solution with an LCO parameter slightly lower than the bifurcation point to ensure that all the eigenvalues are negative.

We enforce an intersection angle constraint that the fitted bifurcation diagram curve shall intersect with the x axis in 90° as shown in Fig. 2. In addition, the curve shall also go through the three sampling points. Then, we compute the slope of a fitting curve and determine the stability using Eq. (24).

The bifurcation diagram is approximated using a third-order polynomial,

$$a\hat{\alpha}^3 + b\hat{\alpha}^2 + c\hat{\alpha} + d = \mu, \quad (25)$$

where a , b , c , and d are coefficients to be determined by the three sampling points and the intersection angle constraint. Three sampling points,

$$(\mu_0, \hat{\alpha}_0), (\mu_-, \hat{\alpha}_-), (\mu_+, \hat{\alpha}_+), \quad (26)$$

where $(\mu_0, \hat{\alpha}_0)$ denotes the parameters with the original LCO point, and $(\mu_-, \hat{\alpha}_-)$ and $(\mu_+, \hat{\alpha}_+)$ denotes parameters from two neighboring points, are considered. One additional constraint for the third-order polynomial fitting is that the slope $d\hat{\alpha}/d\mu$ at $\hat{\alpha} = 0$ shall be zero. The slope constraint at the intersection can be satisfied by

$$c = 0. \quad (27)$$

The remaining coefficients are found by solving the following equation

$$\begin{bmatrix} \hat{\alpha}_-^3 & \hat{\alpha}_-^2 & 1 \\ \hat{\alpha}_0^3 & \hat{\alpha}_0^2 & 1 \\ \hat{\alpha}_+^3 & \hat{\alpha}_+^2 & 1 \end{bmatrix} \begin{bmatrix} a \\ b \\ d \end{bmatrix} = \begin{bmatrix} \mu_- \\ \mu_0 \\ \mu_+ \end{bmatrix}. \quad (28)$$

The stability criterion from Eq. (24) can then be written as

$$g_{\text{stab}} = 3a\hat{\alpha}_0^2 + 2b\hat{\alpha}_0 > \hat{g}, \quad (29)$$

where g_{stab} is the stability measure. As mentioned before, \hat{g} is a non-negative parameter that can be used to further stabilize the system.

5 Derivative computation

For PDE constrained gradient-based optimization, in particular where the function evaluation is expensive, the derivatives must be computed efficiently. The adjoint method is ideal for such a task because the computational cost is independent of the number of design variables. In this section, we derive an adjoint-based approach to compute the derivatives of the proposed constraint.

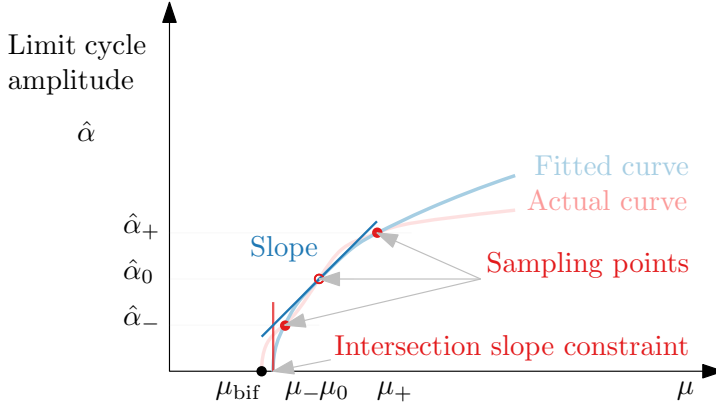


Fig. 2: Stability measure via fitted curve slope.

5.1 Computing $d\mu/d\mathbf{x}$ using adjoint method

To derive the total derivative of a parameter with respect to the design variables, we apply the adjoint method to Eq. (8). The objective, $f(\mu, \omega, \mathbf{w}^n; \mathbf{x})$, is a functional of μ , ω , \mathbf{w}^n , and \mathbf{x} . We further define,

$$\mathbf{q} = \begin{bmatrix} \mu \\ \omega \\ \mathbf{w}^n \end{bmatrix}. \quad (30)$$

Then, differentiating the function of interest and Eq. (8), applying the chain rule, we have

$$\begin{aligned} \frac{df}{d\mathbf{x}} &= \frac{\partial f}{\partial \mathbf{x}} + \frac{\partial f}{\partial \mathbf{q}} \frac{d\mathbf{q}}{d\mathbf{x}}, \\ \frac{d\mathbf{R}}{d\mathbf{x}} &= \frac{\partial \mathbf{R}}{\partial \mathbf{x}} + \frac{\partial \mathbf{R}}{\partial \mathbf{q}} \frac{d\mathbf{q}}{d\mathbf{x}} = 0, \end{aligned} \quad (31)$$

where the second equality is due to the fact that the residual remains zero for any design variable \mathbf{x} . Apply the adjoint method, we have

$$\begin{aligned} \frac{df}{d\mathbf{x}} &= \frac{\partial f}{\partial \mathbf{x}} - \boldsymbol{\psi}^T \frac{\partial \mathbf{R}}{\partial \mathbf{x}}, \\ \frac{\partial \mathbf{R}^T}{\partial \mathbf{q}} \boldsymbol{\psi} &= \frac{\partial f^T}{\partial \mathbf{q}}, \end{aligned} \quad (32)$$

where $\boldsymbol{\psi}$ is the adjoint variable. It is evident that by solving one linear equation, we obtain the derivative with respect to all the design variables.

5.2 Computing $dg_{\text{stab}}/d\mathbf{x}$

The derivative of the constraint $dg_{\text{stab}}/d\mathbf{x}$ is computed using Eq. (28) and Eq. (29), and Eq. (32). We use the adjoint equation Eq. (32) by setting the entries of the $\boldsymbol{\mu}$ as

the function of interest f . It can be computed using the chain rule

$$\frac{dg_{\text{stab}}}{dx} = \frac{dg_{\text{stab}}}{dc} \frac{dc}{d\boldsymbol{\mu}} \frac{d\boldsymbol{\mu}}{dx}, \quad (33)$$

where

$$\mathbf{c} = \begin{bmatrix} a \\ b \\ c \\ d \end{bmatrix}, \quad \boldsymbol{\mu} = \begin{bmatrix} \mu_- \\ \mu_0 \\ \mu_+ \end{bmatrix}. \quad (34)$$

The derivatives

$$\frac{dg_{\text{stab}}}{dc}, \quad \frac{dc}{d\boldsymbol{\mu}}, \quad (35)$$

can be evaluated analytically. The most computationally demanding derivative is

$$\frac{d\boldsymbol{\mu}}{dx}. \quad (36)$$

It can be computed by applying the above adjoint method three times, independent of the number of design variables. It is also possible to use the adjoint method to compute $d\hat{\alpha}/d\boldsymbol{\mu}$. However, this makes the computation of its derivative challenging because it requires a second-order adjoint method to compute design variable derivatives, which is expensive. The proposed fitting method circumvents this by formulating the constraint in terms of $\boldsymbol{\mu}$ instead of its derivative.

6 Numerical results

In this section, we first verify the analysis and derivative computation capability of the proposed method in Section 6.1. Then, in Section 6.2, we consider a simple dynamical system problem where the initial instability is suppressed and a higher bifurcation parameter is sought. Finally, in Section 6.3, we demonstrate the proposed approach on an aeroelastic problem where we optimize the structural weight and compliance. The data of the problems are available online¹.

6.1 Verification

6.1.1 Stability analysis

In this section, we verify that the proposed fitting method can capture and represent the bifurcation diagram characteristics, and the proposed Eq. (33) can compute its slope accurately. Consider the following analytical dynamical system

$$\begin{aligned} \dot{w}_1 &= (\boldsymbol{\mu} - 1)w_1 - w_2 + w_1^3, \\ \dot{w}_2 &= w_1 + (\boldsymbol{\mu} - 1)w_2 + w_2^3. \end{aligned} \quad (37)$$

¹ https://github.com/SichengHe/LCO_stability_fit_data

In this case, we have $N = 2$, and the number of time instances used to solve the problem is set to $n = 5$. The sampling points are arbitrarily chosen for verification with $(\hat{\alpha}_-, \hat{\alpha}_0, \hat{\alpha}_+) = (0.4, 0.5, 0.6)$. As a reminder the $\hat{\alpha}$ refers to the magnitude of the first DOF, $|\hat{\mathbf{w}}_1|$.

The fitted and the actual curve for the bifurcation diagram are shown in Fig. 3. Overall, there is a good agreement between the two curves, in particular close to the sampling points, but further away at the extreme $\hat{\alpha} = 1$ there is a minimal visible difference. The stability measure, g_{stab} , obtained from the fitted curve using analytic formula, Eq. (29), and by central finite differences, are compared in Table 1. We achieve a 4-digit match for this specific case, demonstrating that the proposed method can accurately capture the underlying physics.

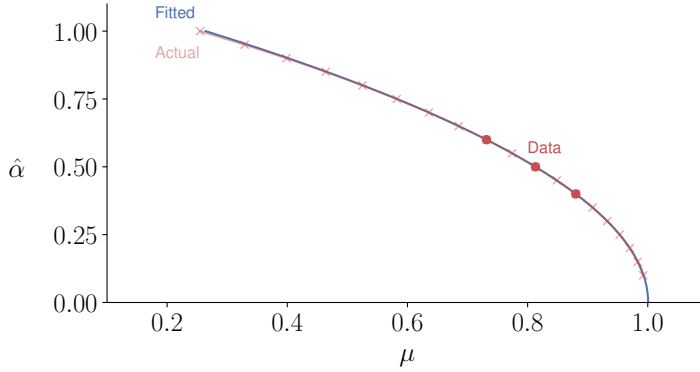


Fig. 3: Stability measure using the proposed method via fitted curve slope compares well with the actual bifurcation map.

Table 1: Verification of stability measure, g_{stab} , computed in the analytic form of the fitted curve and finite difference methods of the actual curve (central difference, step size 2×10^{-7}).

Fitted curve, g_{stab}	Actual curve, FD
<u>-0.74309383</u>	<u>-0.74319293</u>

6.1.2 Derivative verification

In the previous section, we verified the stability measure. In this section, we verify adjoint computation of the derivative of this stability measure, $dg_{\text{stab}}/d\mathbf{x}$. The dynam-

ical system for this task now includes design variables and is defined as

$$\begin{aligned}\dot{w}_1 &= (\mu - x_1)w_1 - w_2 + (2x_1x_2 - 1)w_1^3, \\ \dot{w}_2 &= w_1 + (\mu - x_2)w_2 + (2x_2 - 1)w_2^3.\end{aligned}\tag{38}$$

The prescribed motion magnitude is set to $\hat{\alpha}_0 = 0.5$ and the delta magnitude is the same as before (± 0.1) for the adjacent sampling points. The numerical values are listed in Table 2. We obtain a 4 to 5 digit match for this case, demonstrating that the adjoint method can be used to compute the derivatives accurately.

Table 2: Verification of the stability measure adjoint derivative, $dg_{\text{stab}}/d\mathbf{x}$, compared with the finite difference method.

Design variable	Adjoint	FD
x_1	<u>-0.69548584</u>	<u>-0.69549213</u>
x_2	<u>-1.47698321</u>	<u>-1.47698905</u>

6.2 Instability suppression using gradient-based optimization

Now that we have verified the derivatives, we can perform optimization. The objective is to maximize the LCO parameter, subject to the proposed stability constraint that characterizes the system stability. The optimization problem statement is summarized by Eq. (2). The physical interpretation of this problem is that we want to postpone the onset of bifurcation while ensuring that the LCO branch is stable.

The dynamical system is the same as before, defined in Eq. (38). Also, we need to specify a motion magnitude for the time spectral LCO solver. As before, we set the prescribed motion magnitude to $\hat{\alpha}_0 = 0.5$ and the number of time instances to $n = 5$. The design variable bounds we consider here are set to be $0 \leq \mathbf{x} \leq 1$. The lower bound of the constraint value, \hat{g} from Eq. (29), is set to be 0.1 to make sure the dynamical system is indeed stable. The optimization is conducted using SNOPT (Gill et al., 2002) with the Python interface provided by pyOptSparse (Wu et al., 2020).

It is possible to visualize this problem's design space because there are only two design variables, where we also show the contour plots for the constraint and objective functions are shown in Fig. 4. The major iterations and the optimal point. The optimizer started from the baseline design ($x_1 = 0.3, x_2 = 1$) and found the optimal point to be at $x_1 = 1, x_2 = 0.43$.

The baseline and optimized bifurcation diagrams are shown in Fig. 5. The baseline design has a lower value of μ and turns out to be unstable; the optimized result has a higher value of μ , and is stable. This demonstrates the capability of the algorithm for LCO stability optimization.

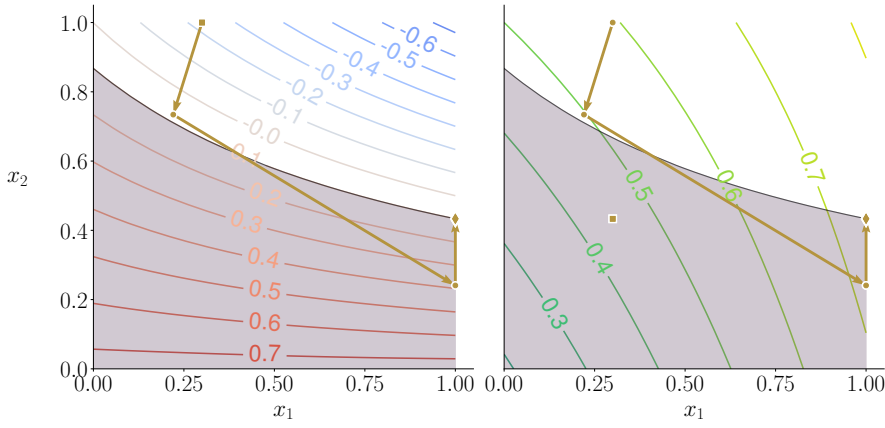


Fig. 4: Stability constraint g_{stab} (left) and the objective function μ (right) contour. The infeasible region is shaded. The brown arrows indicate the path of the optimization. The square mark indicates the starting point and the diamond mark indicates the optimized solution.

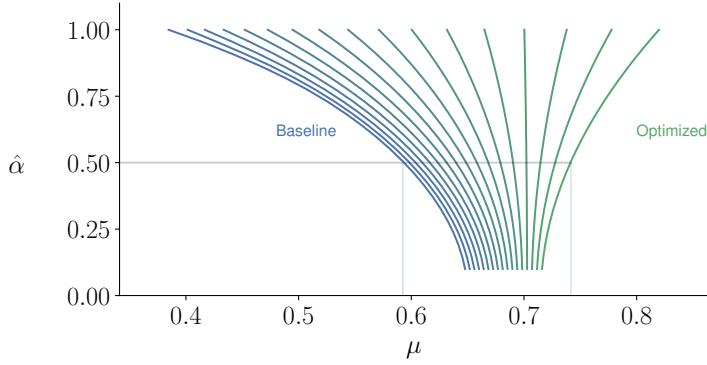


Fig. 5: Baseline, optimized, and intermediate design bifurcation diagrams. The intermediate designs are equally spaced on the straight line linking the baseline and the optimized solution.

6.3 Aeroelastic LCO optimization problem

6.3.1 Problem setup

In this section, we consider an aeroelastic LCO optimization problem. The aeroelastic model used here is adopted from Riso et al. (2021), consisting of a flat-plate typical section in a quasi-steady incompressible potential flow. The dynamical system is given as,

$$\dot{\mathbf{w}} = \mathbf{f}(\mu, \mathbf{w}, \mathbf{x}) = \mathbf{A}(\mu, \mathbf{x})\mathbf{w} + \mathbf{F}_{nl}(\mathbf{w}, \mathbf{x}), \quad (39)$$

where the total function, $\mathbf{f}(\mu, \mathbf{w}, \mathbf{x})$, is composed of a linear coefficient matrix, $\mathbf{A}(\mu, \mathbf{x})$, and a nonlinear vector, $\mathbf{F}_{nl}(\mathbf{w}, \mathbf{x})$.

The state variable vector is defined as

$$\mathbf{w} = \begin{bmatrix} \bar{h} \\ \alpha \\ \dot{\bar{h}} \\ \dot{\alpha} \end{bmatrix}, \quad (40)$$

where \bar{h} and α are a dimensionless plunging and pitching variables, respectively. The design variable vector is defined as

$$\mathbf{x} = \begin{bmatrix} \bar{m} \\ \kappa_\alpha^{(3)} \end{bmatrix}, \quad (41)$$

where \bar{m} is a dimensionless mass per unit length, and $\kappa_\alpha^{(3)}$ is a dimensionless stiffness parameter, which appears later in the nonlinear load.

The linear coefficient matrix is defined as

$$\mathbf{A}(\mu, \mathbf{x}) = \begin{bmatrix} \mathbf{0}_{2 \times 2} & \mathbf{I}_{2 \times 2} \\ -\mathbf{M}_S^{-1}(\mathbf{K}_S + \mathbf{K}_A(\mu, \mathbf{x})) & -\mathbf{M}_S^{-1}\mathbf{D}_A(\mu, \mathbf{x}) \end{bmatrix}. \quad (42)$$

The structural mass and stiffness matrices are defined as

$$\mathbf{M}_S = \begin{bmatrix} 1 & x_\alpha \\ x_\alpha & r_\alpha^2 \end{bmatrix}, \quad \mathbf{K}_S = \begin{bmatrix} \Omega^2 & 0 \\ 0 & r_\alpha^2 \end{bmatrix}, \quad (43)$$

where x_α , Ω , and r_α are constant parameters. The aerodynamic damping and stiffness matrices are defined as

$$\mathbf{D}_A(\mu, \mathbf{x}) = \frac{2}{\bar{m}}\mu \begin{bmatrix} 1 & 0 \\ -\bar{e} & 0 \end{bmatrix}, \quad \mathbf{K}_A(\mu, \mathbf{x}) = \frac{2}{\bar{m}}\mu^2 \begin{bmatrix} 0 & 1 \\ 0 & -\bar{e} \end{bmatrix}, \quad (44)$$

where μ is dimensionless LCO speed, \bar{e} is a constant parameter. The nonlinear load is defined as

$$\mathbf{F}_{nl}(\mathbf{w}, \mathbf{x}) = \frac{r_\alpha^2 \left(\kappa_\alpha^{(3)} \alpha^3 + \kappa_\alpha^{(5)} \alpha^5 \right)}{r_\alpha^2 - x_\alpha^2} \begin{bmatrix} 0 \\ 0 \\ x_\alpha \\ -1 \end{bmatrix} \quad (45)$$

where $\kappa_\alpha^{(5)}$ is another constant dimensionless stiffness parameter. The values of the constants are listed in Table 3.

Table 3: Constant dimensionless parameters for aeroelastic LCO problem.

Property	Description	Value
\bar{e}	Elastic from aerodynamic center offset	0.2
Ω	Plunge-pitch structural frequency ratio	0.5
r_α	Pitch inertia moment	0.3
x_α	Static unbalance per unit length	0.2

Table 4: Parameter values for subcritical and supercritical analysis.

Property	Subcritical	Supercritical
\bar{m}	10.0	10.0
$\kappa_\alpha^{(3)}$	-1.5	1.5
$\kappa_\alpha^{(5)}$	50.0	0.0

6.3.2 Bifurcation diagram

Similar to the example shown in Section 6.1.1, we compare the fitted bifurcation diagram with the true bifurcation diagram for two sets of parameters corresponding to a subcritical and a supercritical behavior. For the time-spectral analysis, the number of time instances is $n = 5$. The prescribed motion center point is set to 5° with a delta of $\pm 4^\circ$. Both cases use the parameters shown in Table 3. And the different parameters used for the subcritical and supercritical cases are shown in Table 4.

The results are shown in Figs. 6 and 7. The fitted curve agrees well with the true curve for the supercritical case. However, for the subcritical case, there is some clear deviation. In the region between $1^\circ \leq \alpha \leq 9^\circ$, the fitted curve is close to the true curve, but for the prescribed motion magnitude $\alpha > 9^\circ$ there is some clear deviation. Since our goal is to improve the stability property of one LCO point at $\alpha = 5^\circ$, the current method is sufficient. Otherwise, if we want to improve the stability of the whole bifurcation diagram, like the current one, it is necessary to add more sampling points and use a higher-order polynomial for the curve fitting. However, the agreement is sufficient for optimization purposes as it captures the overall characteristics of the bifurcation diagram, particularly in the unstable branch. Furthermore, as the optimization progresses, the difference between the fitted and actual bifurcation diagrams should reduce as it approaches a supercritical response, which is well represented by the fitting method.

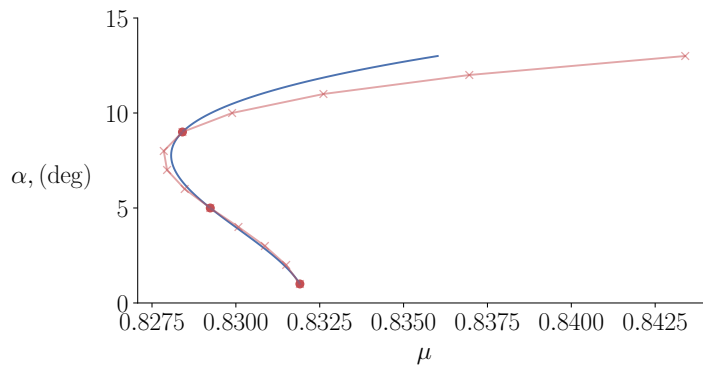


Fig. 6: True (red line) and fitted (blue line) bifurcation diagrams with sampling points (red dots) using parameters from Table 3.

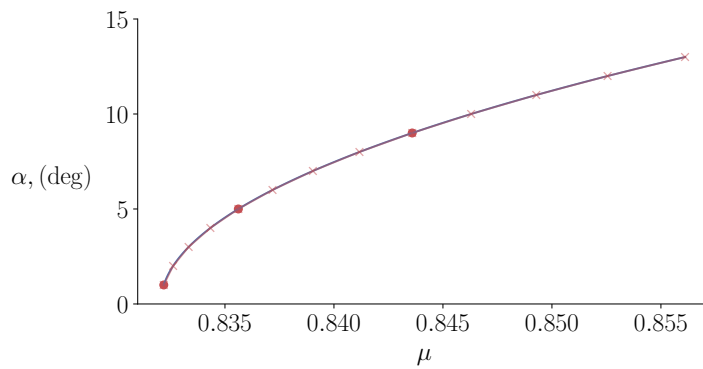


Fig. 7: True (red line) and fitted (blue line) bifurcation diagrams with sampling points (red dots) using parameter from Table 3.

6.3.3 Optimization

With the bifurcation verified, we are ready to conduct an optimization. The optimization problem statement is given in Eq. (46), and is a special form of Eq. (3). The objective is to minimize a function of the structural weight and compliance with respect to the structural weight and cubic stiffness coefficient, subject to the LCO speed

and LCO stability constraints. We prefer a more flexible structure and less mass.

$$\begin{aligned}
& \text{minimize } \bar{m} - \kappa_{\alpha}^{(3)2}, \\
& \text{by varying } \bar{m}, \kappa_{\alpha}^{(3)}, \\
& \text{subject to } g_{\text{stab}}(\bar{m}, \kappa_{\alpha}^{(3)}) \geq \hat{g}, \\
& \quad \mu(\bar{m}, \kappa_{\alpha}^{(3)}) \geq \underline{\mu}, \\
& \quad \underline{\mathbf{x}} \leq \begin{bmatrix} \bar{m} \\ \kappa_{\alpha}^{(3)} \end{bmatrix} \leq \bar{\mathbf{x}}.
\end{aligned} \tag{46}$$

Both constraints are bound, where \hat{g} is the LCO stability lower bound, and $\underline{\mu}$ is the LCO speed lower bound. In this work, the lower bounds are set as follows,

$$\begin{aligned}
\hat{g} &= 0.02, \\
\underline{\mu} &= 0.8.
\end{aligned} \tag{47}$$

The bounds for the design variables are defined as

$$\underline{\mathbf{x}} = \begin{bmatrix} 5 \\ -3 \end{bmatrix}, \quad \bar{\mathbf{x}} = \begin{bmatrix} 15 \\ 0 \end{bmatrix}. \tag{48}$$

As before, the number of time instances is set to $n = 5$, which corresponds to two temporal modes. This choice was shown to be sufficient by He et al. (2021) for an airfoil. For more complex problems where the higher modes play a more significant role, the users can always add more modes at a price of computational time. As before, we conduct the optimization using SNOPT (Gill et al., 2002) with the Python interface provided by pyOptspase (Wu et al., 2020).

The contour plot for the two constraints in the given design space is shown in Fig 8. The initial solution is set to be

$$\begin{bmatrix} \bar{m} \\ \kappa_{\alpha}^{(3)} \end{bmatrix}^{(0)} = \begin{bmatrix} 15 \\ -3 \end{bmatrix}, \tag{49}$$

and the optimized solution is found to be

$$\begin{bmatrix} \bar{m} \\ \kappa_{\alpha}^{(3)} \end{bmatrix}^{(*)} = \begin{bmatrix} 9.25 \\ -0.37 \end{bmatrix}. \tag{50}$$

The initial design has a lower objective function value,

$$\bar{m}^{(0)} - \left(\kappa_{\alpha}^{(3)} \right)^{(0)2} = 6.00. \tag{51}$$

However, this violates the stability constraint; the optimized solution has a higher objective function value of

$$\bar{m}^{(*)} - \left(\kappa_{\alpha}^{(3)} \right)^{(*)2} = 9.11, \tag{52}$$

but this design does not violate the stability constraint. This is evident in Fig. 9, which shows the initial and optimized bifurcation diagrams. Although it has a higher LCO speed, the baseline design went from supercritical to subcritical for the optimized design.

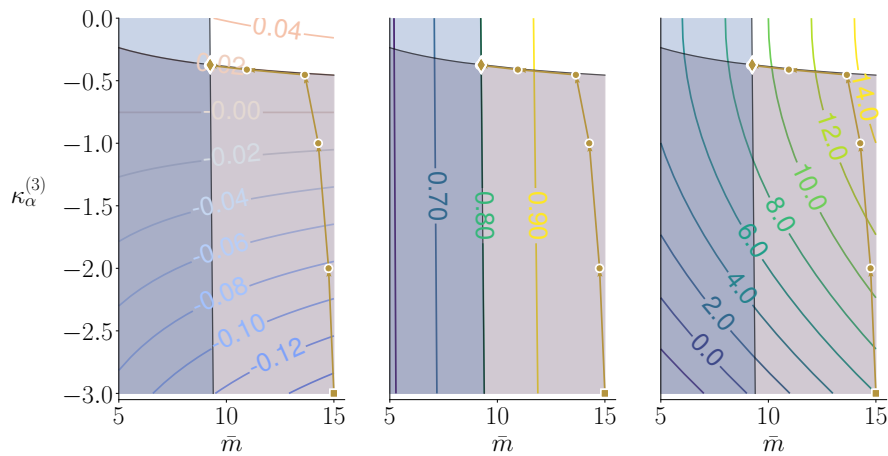


Fig. 8: Contours of the LCO stability constraint g_{stab} (left), the LCO speed constraint μ (middle), and the objective function (right) with the infeasible regions shaded. The brown arrows indicate the path of the optimization. The square mark indicates the starting point and the diamond mark indicates the optimized solution.

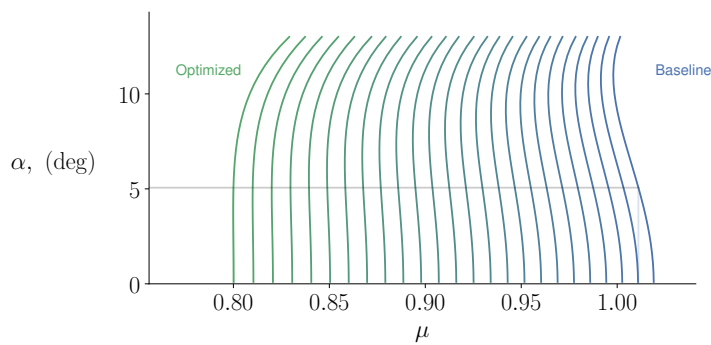


Fig. 9: Baseline, optimized, and intermediate design bifurcation diagrams. The intermediate designs are taken equally spaced on the straight line linking the baseline and the optimized solution.

7 Conclusion

In this paper, we propose a fitting curve-based method as a metric for LCO stability and an adjoint-based derivative computation that can be used for design optimization. The advantage of this method is that the stability metric is computed with only three points, in this case, solved using a time-spectral method, making the approach computationally efficient for estimating the bifurcation diagram. Further, the computational cost of the adjoint approach is independent of the number of design variables. For the analysis, three adjoint solutions are required in computing the total derivative. We demonstrated the proposed method in two problems: (1) An LCO stability constrained LCO parameter optimization problem where we found that the initial instability was suppressed and the optimized solution was stable, (2) An aeroelastic optimization problem with LCO parameter and LCO stability constraints, where the baseline design subcritical behavior was successfully suppressed, resulting in a supercritical optimized design. This method can be used to solve large-scale design optimization problems, such as a flutter speed optimization problem with a stability constraint for an aircraft wing.

Conflict of Interest

The authors declare that they have no conflict of interest.

Data Availability Statement

The numerical implementation of algorithms and results discussed in this work are available in the form of an open-source Python software at the following DOI: [10.5281/zenodo.5992080](https://doi.org/10.5281/zenodo.5992080).

References

- Bauchau OA, Nikishkov YG (2001) An implicit Floquet analysis for rotorcraft stability evaluation. *Journal of the American Helicopter Society* 46(3):200
- Cao Y, Li S, Petzold L, Serban R (2003) Adjoint sensitivity analysis for differential-algebraic equations: The adjoint DAE system and its numerical solution. *SIAM Journal on Scientific Computing* 24(3):1076–1089
- Chicone C (2006) *Ordinary Differential Equations with Applications*. Springer New York
- Floquet G (1883) Sur les équations différentielles linéaires à coefficients périodiques. *Annales scientifiques de l'École normale supérieure* 12:47–88
- Friedmann P, Hammond CE, Woo TH (1977) Efficient numerical treatment of periodic systems with application to stability problems. *International Journal for Numerical Methods in Engineering* 11(7):1117–1136
- Gill PE, Murray W, Saunders MA (2002) SNOPT: An SQP algorithm for large-scale constrained optimization. *SIAM Journal of Optimization* 12(4):979–1006

- Grizzle J, Abba G, Plestan F (2001) Asymptotically stable walking for biped robots: analysis via systems with impulse effects. *IEEE Transactions on Automatic Control* 46(1):51–64
- He S, Jonsson E, Mader CA, Martins JRRA (2019a) Aerodynamic shape optimization with time spectral flutter adjoint. In: 2019 AIAA/ASCE/AHS/ASC Structures, Structural Dynamics, and Materials Conference, American Institute of Aeronautics and Astronautics, San Diego, CA
- He S, Jonsson E, Mader CA, Martins JRRA (2019b) A coupled Newton–Krylov time-spectral solver for wing flutter and LCO prediction. In: AIAA Aviation Forum, Dallas, TX
- He S, Jonsson E, Mader CA, Martins JRRA (2021) Coupled Newton–Krylov time-spectral solver for flutter and limit cycle oscillation prediction. *AIAA Journal* (In press)
- Huang D, Rokita T, Friedmann PP (2018) Integrated aerothermoelastic analysis framework with application to skin panels. *AIAA Journal* 56(11):4562–4581
- Jameson A (1988) Aerodynamic design via control theory. *Journal of Scientific Computing* 3(3):233–260
- Jonsson E, Riso C, Lupp CA, Cesnik CES, Martins JRRA, Epureanu BI (2019) Flutter and post-flutter constraints in aircraft design optimization. *Progress in Aerospace Sciences* 109:100,537
- Kenway GW, Kennedy GJ, Martins JRRA (2014) Scalable parallel approach for high-fidelity steady-state aeroelastic analysis and adjoint derivative computations. *AIAA Journal* 52(5):935–951
- Kenway GW, Mader CA, He P, Martins JRRA (2019) Effective adjoint approaches for computational fluid dynamics. *Progress in Aerospace Sciences* 110:100,542
- Knoll DA, Keyes DE (2004) Jacobian-free Newton–Krylov methods: a survey of approaches and applications. *Journal of Computational Physics* 193(2):357–397
- Lasagna D (2018) Sensitivity analysis of chaotic systems using unstable periodic orbits. *SIAM Journal on Applied Dynamical Systems* 17(1):547–580
- Li H, Ekici K (2019) Aeroelastic modeling of the AGARD 445.6 wing using the harmonic-balance-based one-shot method. *AIAA Journal* 57(11):4885–4902
- Manchester IR, Tobenkin MM, Levashov M, Tedrake R (2011) Regions of attraction for hybrid limit cycles of walking robots. *IFAC Proceedings Volumes* 44(1):5801–5806
- Riso C, Ghadami A, Cesnik CES, Epureanu BI (2020) Data-driven forecasting of postflutter responses of geometrically nonlinear wings. *AIAA Journal* 58(6):2726–2736
- Riso C, Cesnik CES, Epureanu BI, Teufel P (2021) A post-flutter response constraint for gradient-based aircraft design optimization. In: AIAA Aviation 2021 Forum, American Institute of Aeronautics and Astronautics
- Seyranian A, Solem F, Pedersen P (2000) Sensitivity analysis for the floquet multipliers. In: 2000 2nd International Conference. Control of Oscillations and Chaos. Proceedings (Cat. No.00TH8521), IEEE
- Shi Y, Mader CA, He S, Halila GLO, Martins JRRA (2020) Natural laminar-flow airfoil optimization design using a discrete adjoint approach. *AIAA Journal* 58(11):4702–4722

- Shimizu YS, Fidkowski K (2016) Output error estimation for chaotic flows. In: 46th AIAA Fluid Dynamics Conference, American Institute of Aeronautics and Astronautics
- Shiriaev A, Freidovich L, Manchester I (2008) Can we make a robot ballerina perform a pirouette? orbital stabilization of periodic motions of underactuated mechanical systems. *Annual Reviews in Control* 32(2):200–211
- Thomas JP, Dowell EH (2019) Discrete adjoint approach for nonlinear unsteady aeroelastic design optimization. *AIAA Journal* 1–9
- Thomas JP, Dowell EH, Hall KC (2002) Nonlinear inviscid aerodynamic effects on transonic divergence, flutter, and limit-cycle oscillations. *AIAA Journal* 40(4):638–646
- Virtanen P, Gommers R, Oliphant TE, Haberland M, Reddy T, Cournapeau D, Burovski E, Peterson P, Weckesser W, Bright J, van der Walt SJ, Brett M, Wilson J, Millman KJ, Mayorov N, Nelson ARJ, Jones E, Kern R, Larson E, Carey CJ, Polat I, Feng Y, Moore EW, VanderPlas J, Laxalde D, Perktold J, Cimrman R, Henriksen I, Quintero EA, Harris CR, Archibald AM, Ribeiro AH, Pedregosa F, van Mulbregt P (2020) SciPy 1.0: fundamental algorithms for scientific computing in python. *Nature Methods* 17(3):261–272
- Wang Q (2013) Forward and adjoint sensitivity computation of chaotic dynamical systems. *Journal of Computational Physics* 235:1–13
- Waugh IC, Kashinath K, Juniper MP (2014) Matrix-free continuation of limit cycles and their bifurcations for a ducted premixed flame. *Journal of Fluid Mechanics* 759:1–27
- Wilkins AK, Tidor B, White J, Barton PI (2009) Sensitivity analysis for oscillating dynamical systems. *SIAM Journal on Scientific Computing* 31(4):2706–2732
- Wu N, Kenway G, Mader CA, Jasa J, Martins JRRA (2020) pyOptSparse: a Python framework for large-scale constrained nonlinear optimization of sparse systems. *Journal of Open Source Software* 5(54):2564
- Xu J, Huang C, Duraisamy K (2020) Reduced-order modeling framework for combustor instabilities using truncated domain training. *AIAA Journal* 58(2):618–632
- Yildirim A, Kenway GWK, Mader CA, Martins JRRA (2019) A Jacobian-free approximate Newton–Krylov startup strategy for RANS simulations. *Journal of Computational Physics* 397:108,741